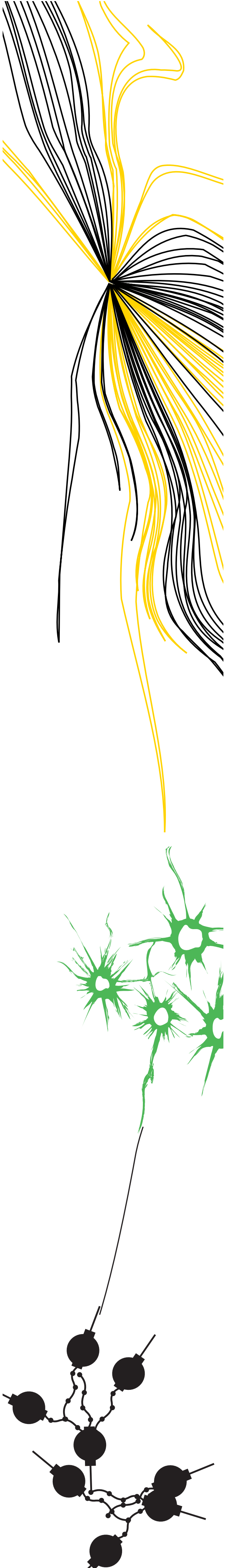

RAM
ROBOTICS
AND
MECHATRONICS

3D RECONSTRUCTION OF THE DEFORMED BREAST SURFACE FROM AUTONOMOUSLY ACQUIRED ULTRASOUND IMAGES

S.M.M.D.P. (Sheona) Sequeira

MSC ASSIGNMENT

Committee:
dr. F.J. Siepel, MSc
A.G. de Groot, MSc
dr. N. Strisciuglio

July 2021

041RaM2021
Robotics and Mechatronics
EEMathCS
University of Twente
P.O. Box 217
7500 AE Enschede
The Netherlands

UNIVERSITY OF TWENTE. | TECHMED CENTRE
UNIVERSITY OF TWENTE. | DIGITAL SOCIETY INSTITUTE

3D Reconstruction of the deformed Breast Surface with Autonomously acquired Ultrasound Images

Sheona M. M. D. P. Sequeira
Master Electrical Engineering
University of Twente
Enschede, The Netherlands

***Abstract*—Research is currently being done to improve the sensitivity of breast cancer detection by fusing breast volumes acquired from Magnetic Resonance (MR) Imaging and Ultrasound (US) together. Attributing to the highly restrictive nature of the MR environment, both these image volumes are acquired separately. Hence, making a surface reconstruction an essential requirement for performing accurate fusion. In the current implementation, the surface reconstruction is done with the help of a stereo camera and multi-modality markers that are placed on the breast surface. The positions of these markers, however, need to be maintained constant throughout the procedure, thus posing a challenge in a clinical environment. The purpose of this study is to perform the 3D breast surface reconstruction with autonomously acquired US images. The surface reconstruction algorithm is built by exploiting the transition area between the instances of contact and no contact between the US probe and the breast surface. Validation of the algorithm is done on a realistic breast phantom by performing several experiments with varying amounts of desired contact between the two surfaces as well as with varying US probe orientations. On taking the average of 10 scans per experiment, a minimal error of 3.87 mm was obtained when the US probe was in horizontal orientation and with a desired amount of contact of 30% of the US probe width. This algorithm has potential to eliminate the need of marker and a camera scan, making the setup for performing MR/US fusion more feasible for clinical implementation.**

I. INTRODUCTION

Female breast cancer is the fifth leading cause of cancer mortality worldwide with an incidence rate of 11.7% [1]. Literature stipulates that the early detection of cancer results in a reduction in the mortality rate and an increase in life expectancy [2], [3].

With advancement in technology, early detection of breast cancer has become a reality [3]. The imaging modality, mammography, is the recognised gold standard for breast cancer detection. However, its sensitivity of detection is dependent on the breast density; having a sensitivity and specificity as high as 80% and 97-99% respectively in normal breast tissues to a sensitivity as low as 40% in extremely dense breasts [4], [5]. Furthermore, research indicates that breast density in itself is an independent risk factor for cancer [6], thus making it vital to improve the cancer detection rate in dense breast tissues.

The sensitivity of detection is currently improved by supplementing mammography with imaging modalities that are unaffected by breast density such as Magnetic Resonance Imaging (MRI) and Ultrasound (US) [6]–[8]. Having a sensitivity of approximately 99%, MRI can detect small cancerous lesions. However, it has a highly variable specificity ranging between 28-100% [3]. US imaging, on the other hand, is an easily available, cheap, real-time and non-invasive imaging modality. In a study done by Sim et. al. [9] on women with familial risk of breast cancer, it has been demonstrated that US imaging has a sensitivity and specificity of 83.3% and 65.5% respectively. Nonetheless, both these imaging modalities have certain limitations. As a result of the strong magnetic fields emitted while performing an MRI, specific MR friendly instruments need to be used. This leads to a procedure that is expensive and is at the cost of patient comfort [10]. Additionally, MRI requires the injection of a contrasting medium into the breast tissue for aid in boundary detection. The main limitation of US imaging is its non-reproducibility and high dependence on a clinician's expertise, both of which have been overcome in many studies by using Automated Breast US [11]–[13]. Moreover, the sensitivity of detection in US imaging also depends on the size of the cancerous lesion being scanned.

Research is also being conducted into combining the characteristics of the highly sensitive MR with the real time US through a technique known as MR/US fusion [10], [14], [15]. The MRI and US Robotic Assisted Biopsy project (MURAB) aims at improving the precision and effectiveness of performing a biopsy for cancer detection by using MR/US fusion. This is achieved by obtaining a pre-operative MR image that is fused together with autonomously acquired US images [16]. Fusion of the two volumes helps with the localisation of small lesions (which are only detected in an MR image) in an US image. Attributing to the restrictive nature of the MR environment, both these image volumes are acquired separately with the patient lying in a prone position. Furthermore, due to the elastic properties of the breast tissue, there is a difference in the amount of surface deformation that occurs while acquiring both the volumes. Thus, a breast surface reconstruction is an essential requirement for ensuring accurate fusion of the two volumes and for calculating the amount of breast shape deformation between them.

Currently, as part of the MURAB workflow, the 3D surface reconstruction is performed with the help of a depth camera (like a stereo camera) [17]. Due to the lack of high contrast features on the skin surface, five multi-modality markers are placed as landmarks on the breast surface. By tracking the positions of these markers with the help of a camera scan, it is possible to locate the breast in the US environment. Subsequent registration of the tracked data with the MR volume results in a 3D surface reconstruction of the breast. In order to ensure accurate registration of the tracked markers with the MR data, the markers need to be placed at well-determined distances from each other, with their positions maintained constant throughout the procedure. Changes in the marker positions could cause errors in the camera reconstruction, resulting in registration inaccuracies and requiring the entire procedure to be repeated. The use of such multi-modality markers thus pose a challenge in a clinical setup.

In this study, we propose an algorithm to perform the 3D breast surface reconstruction from autonomously acquired US images. 3D surface reconstruction with the help of US images would eliminate the need to perform a camera scan as well as the requirement of multi-modality markers. Thus resulting in a reduction in the overall number of sensors used in the workflow. Additionally, 3D US surface reconstruction would also improve the quality of breast shape detection, thereby improving the overall quality of the MR/US fusion. On the whole, the 3D US surface reconstruction would improve the current MURAB workflow and make the setup more feasible for clinical use. Breast surface reconstruction is achieved by exploiting the transition area from contact to no contact between the US probe and the breast surface (acoustic/non acoustic coupling). This transition area has been emphasised in the confidence maps that have been computed from US images as part of the previous work [16]. Validation of the reconstruction algorithm is done by performing several experiments on a realistic breast phantom.

In section II, a detailed explanation of the Methods of Implementation can be found, followed by the Experimental Setup and the Results in section III. A Discussion about the results is done in section IV and the Conclusion of this study is highlighted in section V. Possible suggestions for Further Research are mentioned in section VI.

II. METHODS

A complete system overview can be found in figure 1. The patient is positioned prone on the bed with the breast to be scanned hanging freely through a hole. The robot has an US probe attached to its end-effector and is stationed such that it can be in contact with the breast.

The robot moves around the breast surface on a pre-defined reference trajectory to acquire US images. This reference trajectory includes a series of poses of the robot along the breast surface and is determined by making an assumption about the shape of the breast. The acquired US images are then used to compute confidence maps, that provide an indication on which US scanlines are in contact with the breast surface.

Due to the complexity of the breast shape and in order to correct for the inaccuracies in the assumption used for defining the reference trajectory, the robot is controlled using Confidence Driven Control (CDC) which takes the confidence maps as input and produces an output that accordingly adjusts the pose of the robot.

Moreover, since a confidence map highlights the contact information between the US probe and the breast surface, it also plays a vital role in breast surface reconstruction.

Each subsystem in the system overview (figure 1) is described in detail in sections II-A to II-D.

A. Reference Trajectory

The generation of a reference trajectory is done with the assumption that the breast shape in a prone position is comparable to an inverted dome structure. Furthermore, it involves the creation of a scanning path that comprises of a series of homogeneous matrices representing a pose of the robot along the breast surface (expressed in robot base frame). Accordingly, to ensure contact between the US probe and the breast surface at all times, a rotation about two axes (the x and z axes of the robot base frame) has to be taken into account.

This generated reference path is then served as input to the robot.

B. Confidence Map

The concept of US confidence maps has been developed by Karamalis et. al. [18] and has been optimised in the previous work, Wellerweerd et. al. [16]. An US confidence map, C, of dimensions $M \times N$, estimates a continuous per pixel confidence for the information depicted in the US image and is computed by using a random walk framework that has the following constraints [18], [19]:

- The top row of the confidence map represents the virtual transducer elements and is assigned a confidence 1
- The bottom row of the confidence map represents the absorption region and is assigned a confidence 0
- The rest of the rows have a confidence value ranging between 0 and 1 and are calculated by using US specific constraints

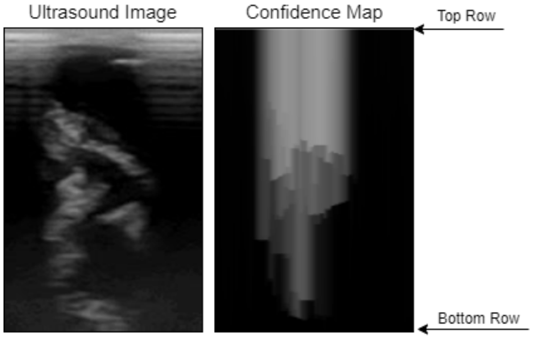

Figure 2: An illustration of (Left) US image (Right) Confidence Map. In the confidence map, it can be seen that the top row elements are assigned a confidence 1, and the bottom row assigned a value 0

These constraints are implemented with the help of three free parameters (α, β, γ): α represents the attenuation coefficient, β is responsible for the accuracy of the segmentation

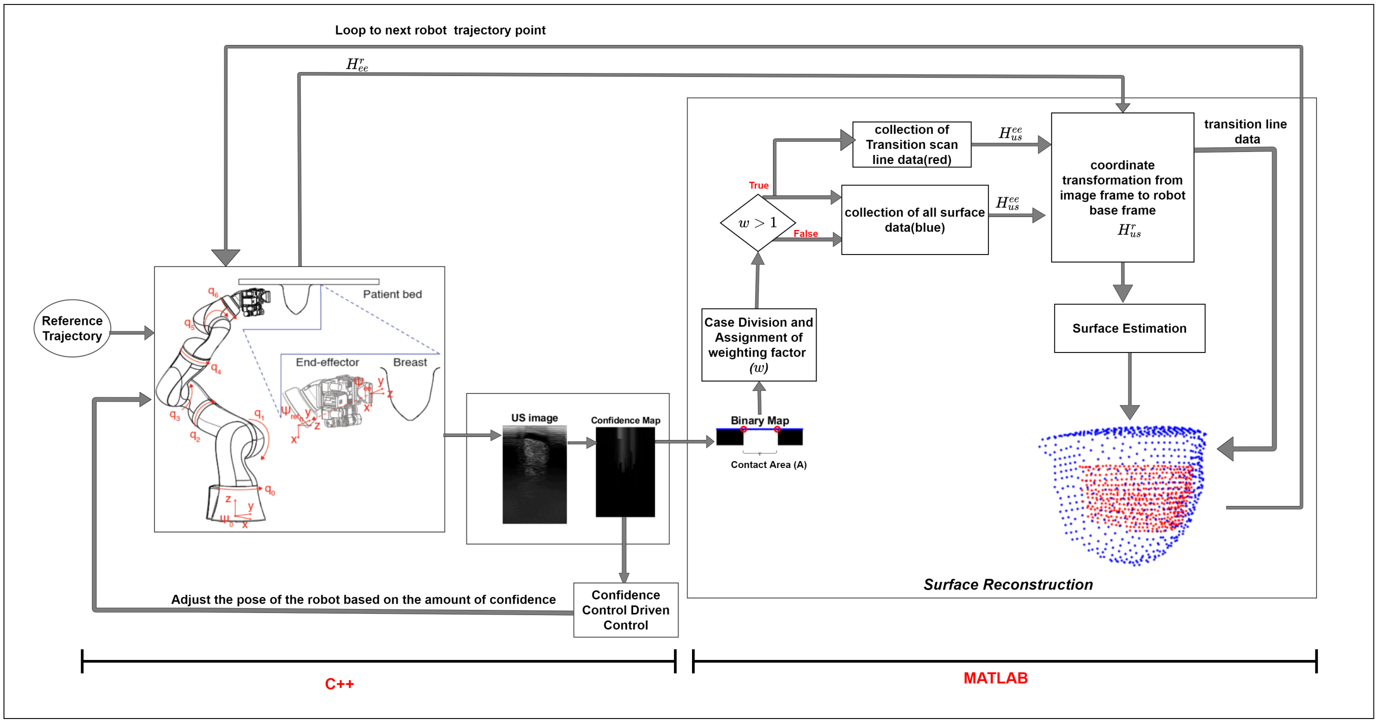

Figure 1: System Overview: (Starting from left to right) The Robotic Manipulator is located under the bed in contact with the patient's breast hanging in a prone position. An input trajectory is offered to the robot. Confidence Maps computed from US images serve as input to CDC and Surface Reconstruction of the Breast. The software (coding language) used is highlighted below the sections.

and γ is the penalty parameter that penalises the confidence in the horizontal and diagonal directions. An illustration of a confidence map is shown in figure 2 and a complete explanation about confidence maps as well as the effects of the varying free parameters on the map can be found in appendix A.

In our study, these free parameters are optimised for performing breast surface reconstruction.

An US confidence map emphasises the regions of acoustic coupling, further providing information about which US scanlines are in contact with the breast and the rough location of the breast surface. As a result of which, the confidence map serves as input to both CDC and the surface reconstruction algorithm.

C. Confidence Driven Control

Due to the difference between the actual shape of the breast and the assumption made (to generate the reference trajectory), some amount of error will be present in the trajectory. These errors are overcome by using the CDC method to control the robot.

CDC takes the confidence maps as well as a desired amount of contact (C_s) as input. With the help of a PD controller, the method results in an output that adjusts the pose of the robot whenever the amount of contact is greater than or less than the desired C_s. In this way, CDC ensures the occurrence of a minimal amount of breast surface deformation and corrects for the reference trajectory errors.

This control method has been validated as part of the previous work [20].

D. Surface Reconstruction

Surface reconstruction, is performed by post processing the confidence maps in a series of steps explained in detail in sections II-D1 to II-D5. The transition between instances of acoustic and no acoustic coupling provides an indication on where the breast surface is located, thus making it vital to enhance the contrast between these regions. This is achieved by binarising the optimised confidence maps. The next step in the reconstruction algorithm involves the division of the binary images into different cases based on the nature of contact between the breast and the US probe. This division is mainly used to validate the choice of the thresholding method used in binarisation. Furthermore, dependent on the amount of acoustic coupling, the binary images are also assigned a weighting factor. The transition scanline information is then collected from only the images with a weighting factor above 1. While, independent of the assigned weighting factor, all the surface scanline information is collected from every image and is used in a later stage to assist with surface estimation. Since the US scanning is performed in the robot base frame, the information acquired from each image also needs to be transformed to the robot based frame in order to create a 3D breast surface representation. Subsequently, a surface estimate is created for the cases when a transition scanline is not determined by using the surface information collected from the binary images and the assigned weights. With the help of the transformed transition scanline information as well as the surface estimates, a dense 3D reconstruction of the breast can then be created.

1) Image Binarisation: Image binarisation involves the conversion of per pixel confidence map data into binary data [21]. A basic technique of binarisation is *thresholding* which is performed using equation (1), where B and T represent the output binary image and threshold respectively and (i, j) represent the pixel indices.

$$B(i,j) = \begin{cases} 1, & \text{if } C(i,j) > T \\ 0, & \text{otherwise} \end{cases} \tag{1}$$

5 different thresholding methods namely Basic Automatic Thresholding [22], Otsu's Global Thresholding [23], Modified Otsu's Thresholding [24], Bi-level Thresholding [25] and Tsallis entropy [26] have been validated in this study.

In a binary image, B, acoustic coupling is represented by the pixels assigned a value 1, while the other pixels indicate no acoustic coupling. This clear representation of (no) acoustic coupling facilitates the effortless extraction of surface information from the image. Each of the vertical lines (columns) in the binary image represent an individual US scanline.

2) Case Division and Assignment of Weighting factor: Based on the nature of contact between the two surfaces, the binary images are divided into five cases. This case division is mainly used for the validation of the choice of the thresholding method. A description of each case can be found below and an illustration can be seen in table I.

(a) *No Contact:* The US probe is not in contact with the breast. Indicating that the breast surface lies below the current US probe position when looking at the z component in the US probe end effector frame.
(b) *Partial Contact:* Only a section of the probe starting from one of its short edges is in contact with the breast.
(c) *Complete Contact:* The entire US probe is in contact with the breast. During the occurrence of this case, the breast shape undergoes maximum deformation, thus reflecting that in the undeformed state, the breast surface would be located above the position of the US probe when looking at the z component in the US probe end effector frame.
(d) *Contact centered around the Centre Scanline:* The contact between the breast and the US probe is centred around the mid point of the US probe, thus ensuring an equal amount of contact between the breast and the US probe on either side of the scanline.
(e) *Interrupted Contact:* Since the breast surface is not perfectly hemispherical in shape, there are some instances when the US probe makes contact with two distinct sections of the breast at the samt time.

Table I: Illustration of the different cases based on the nature of contact

Nature of Contact	Illustration	US image	Confidence Maps
No Contact			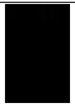
Partial Contact	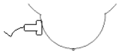	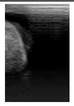	
Complete Contact			
Contact centered around the Center Scanline		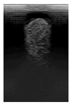	
Interrupted Contact		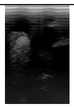	

Upon validation of the different thresholding methods (figure 13, appendix B), the most efficient method is further modified to be robust against segmentation errors by eliminating brief transitions of ones and zeros.

Only the top few layers (20 rows) of B will be processed since literature stipulates that the skin layer lies in the top $0.5-2$ mm in a breast tissue [27]. The shortened binary image with size $M' \times N$ is represented by B in the rest of the paper.

With the help of B, the mean (B_{mean}) of each scanline can be computed using equation (2). The amount of contact between the breast and the US probe (A), which is represented by the regions of acoustic coupling in a binary image, can then be determined from the instances when B_{mean} is equal to 1.

$$B_{\text{mean}} = \frac{1}{M'} \cdot \sum_{i}^{M'} B \tag{2}$$

Due to the elastic properties of the breast, tissue deformation is inevitable when the breast is in contact with the US probe. With an increase in the amount of contact between the breast and the US probe, the amount of tissue deformation caused by contact forces increases. Thus, depending on the value of A, a weighting factor w computed using equation (3) is assigned to each image.

$$w = \begin{cases} 1 & \text{if } A = 1 \\ 0, & \text{else if } A = 0 \\ \frac{1}{A^2}, & \text{otherwise} \end{cases} \tag{3}$$

3) Collection of Surface Information: Using the knowledge of B_{mean} obtained from equation (2), the transition scanline between acoustic and no acoustic coupling can be determined. As seen in the illustration of the cases in table I, a transition scanline can be obtained for all images except when there is complete or no contact between the two surfaces. This is because in these cases, the binary image is represented by all ones or zeros respectively.

All the surface scanline information from each image in the scanning trajectory needs to be collected in order to assist in computing an estimate for these exception cases. Furthermore, dependent on whether the scanline information represents acoustic or no acoustic coupling, it is assigned a constant as is given in equation (4).

$$R(j) = \begin{cases} -1 & \text{if } B_{\text{mean}}(j) = 1 \\ +1, & \text{otherwise} \end{cases} \tag{4}$$

where $j = 1.....N$ with N depicting the total number of scanlines (number of columns).

4) Coordinate Transformation from US Image frame to Robot Base frame H^{r}_{us}: Extracted from an image, the surface information collected in the previous stage is expressed in 2D. In order to create a 3D representation of the data, a coordinate transformation from US image frame to the robot base frame needs to be performed. This is done as follows:

(a) *Coordinate transformation from US Probe End Effector Frame to Robot Base Frame H^{r}_{ee}*: The coordinate transformation from US end effector frame to robot base frame, H^{r}_{ee}, can be computed by applying Brockett's exponential formula as in equation (5) on the robot joint configuration (q) at each step of data acquisition.

$$H^{\text{r}}_{\text{ee}}(q_1, q_2, .., q_{\text{n}}) = e^{\tilde{\hat{T}}^{0,0}_{1} q_1} .... e^{\tilde{\hat{T}}^{\text{n}-1,\text{n}-1}_{\text{n}} q_{\text{n}}} \cdot H^{\text{r}}_{\text{ee}}(0) \tag{5}$$

where $\tilde{\hat{T}}$ and $H^{\text{r}}_{\text{ee}}(0)$ represents the unit twist and pose of the robot respectively both obtained in reference configuration and n represents the degree-of-freedom (DoF) of the robot.

The US probe end effector frame is computed with respect to the center of the US probe (center scanline).

(b) *Conversion of US image data from pixels to meter scale*: The surface information extracted from an US image is expressed in pixels. However, the robot configuration is given in meter scale. Thus, so as to successfully perform coordinate transformation, the image data needs to be converted to meter scale. This is achieved using equation (6), where in p_{pix} and d represent the current scanline in pixels and the US probe width (in meters) respectively.

$$pt = p_{\text{pix}} \cdot \frac{d}{N} \tag{6}$$

The center scanline, c, can also be expressed in the meter scale by using equation (6).

(c) *Coordinate Transformation from US Image Frame to US Probe End Effector Frame $H^{\text{ee}}_{\text{us}}$*:

The US images are acquired such that the x and z axes of the US probe are aligned with the image x and y axes respectively. Thus on conversion to the US probe end effector frame, there will be no y component.

The coordinate transformation, $H^{\text{ee}}_{\text{us}}$ is then calculated using equations (7) and (8) where pt_{x} and c_{x} represent the x coordinate of the surface point pt and the centre scanline point c respectively and $\delta_{\text{z}} = 0$ since both p_{z} and c_{z} are equal to 1 as seen in figure 3.

$$\begin{gathered} \delta_{\text{x}} = pt_{\text{x}} - c_{\text{x}} \\ \delta_{\text{z}} = 0 \end{gathered} \tag{7}$$

$$H^{\text{ee}}_{\text{us}} = \begin{bmatrix} 1 & 0 & 0 & \delta_{\text{x}} \\ 0 & 1 & 0 & 0 \\ 0 & 0 & 1 & 0 \\ 0 & 0 & 0 & 1 \end{bmatrix} \tag{8}$$

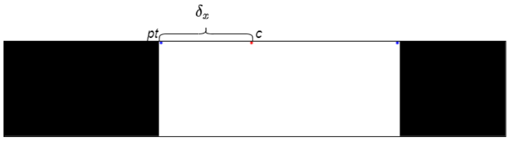

Figure 3: Section of the binary image representing the skin surface. c and pt represent the coordinates of the centre (red) and transition (blue) scanline respectively

(d) *Coordinate Transformation from US Image Frame to Robot Base Frame H^{r}_{us}*: The coordinate change is obtained by the multiplication of the two poses H^{r}_{ee} and $H^{\text{ee}}_{\text{us}}$ as in equation (9).

$$H^{\text{r}}_{\text{us}} = H^{\text{r}}_{\text{ee}} H^{\text{ee}}_{\text{us}} \tag{9}$$

5) Surface Estimation: Since no transition data can be acquired for the cases with complete or no contact between the US probe and the breast surface, a surface estimation is computed. This is done with the help of the assigned constants, weights and transformed surface data acquired from each image.

The range of points used to calculate the estimate is selected based on the weights such that it follows a valley representation with the minimum point representing the weight of the surface point for which an estimate is to be computed. After selection of the desired range of surface points, the mean value of all the selected points assigned a negative and positive constant are computed separately. The surface estimate is then taken to be the average of the two mean points.

If a transformed surface point has been assigned contradicting constant values, the value obtained from the image with a higher weight is considered.

Finally, the point cloud is generated with the help of two sets of point data: the transformed transition point data acquired from the binary images and the calculated surface estimates.

During data acquisition and processing, some amount of noise is induced into the point cloud, thus making smoothing essential. The clearly distinguishable outliers are eliminated using k-nearest neighbours outlier removal approach, where in points with low local density are eliminated. The data is then smoothened using a single iteration Laplacian Smoothing method [28]. Additional filtering is done by eliminating the points that are a short distance away (less than 1 mm) from each other and have a relatively lower assigned weight.

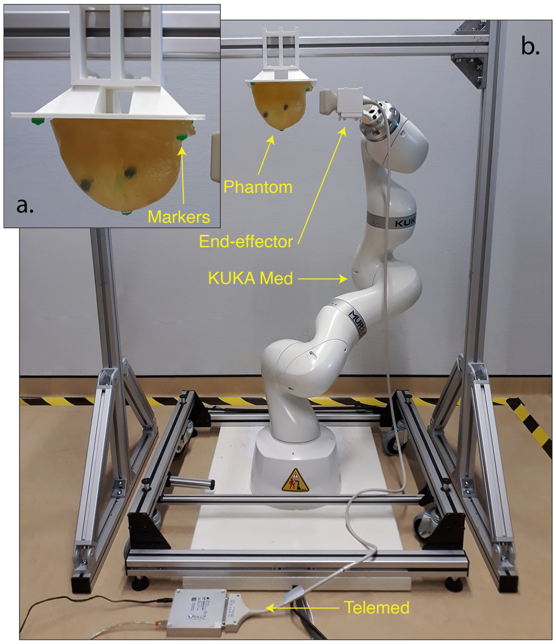

Figure 4: Experimental Setup: a) A zoomed in version of the breast phantom with the US end effector in Vertical Orientation. b) The 7DoF KUKA Med Robot with a Telemed linear US probe attached to its end effector stationed to be near the breast phantom.

III. EXPERIMENTS AND RESULTS

A. Experimental Setup

The experimental setup, as seen in figure 4, comprises of a 7 DoF robotic manipulator, KUKA LBR Med 7 800 (KUKA GMBH, Germany), that has a Telemed linear US probe (Telemed, UAB, Lithuania) attached to its end effector. The US probe is connected to a MicrUS EXT-1H (Telemed UAB, Lithuania) with which US images are streamed at an update rate of 40 Hz.

A breast phantom is produced from the surface reconstruction of a breast MRI taken in a prone position. The characteristics of a real breast tissue are replicated into the phantom by using two moulds, an outer mould depicting the breast shape and an inner mould. The dimensions of the inner mould are selected such that there is a 5 mm gap between both the moulds. This hollow region is filled with a PVCP/Plasticizer $(100\%/0\%)$ mixture (Bricoleure, France) in order to represent the skin layer. The rest of the volume is then filled with a combination of PVCP/Plasticizer $(100\%/0\%)$ and PVCP/Plasticizer $(70\%/30\%)$ strands.

Software: As shown in figure 1, the surface reconstruction algorithm is developed using MATLAB 2021a. The rest of the procedure is built using C++.

B. Experiments

10 scans are performed for each varying US probe orientation and C_s value taken as input in CDC. The C_s values were varied between 15-20% of the set confidence ($C_\mathrm{s} = 0.5$) used in previous work [20]. At the start of each scan, the robot is positioned such that the US probe has little to no contact with the breast surface. A section covering approximately 75° of the entire breast (from the starting point) is scanned.

An overview of the experiments performed is given in table II.

Table II: Experimental Overview: 10 scans performed with each orientation and C_s value. The range is selected such that instances with a small amount of deformation are included.

Probe Orientation	**Confidence Driven Control**	
	C_s	*Range*
Horizontal / Vertical	0.3	0.2-0.4
	0.5	0.2-0.7
	0.65	0.2-0.8

C. Results

The desired experiments were conducted successfully. All the 3D surface plots are presented together with the ground truth, MR|Stereo Camera surface reconstruction. A single instance for the 3D breast surface reconstruction with the probe in the horizontal and vertical orientations is visualised in figure 5.

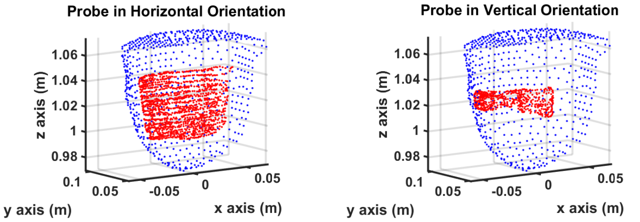

Figure 5: Dense US Surface Reconstruction (red dots) for a section of the breast superimposed with the ground truth MRI|Stereo Camera Reconstruction (blue). Both 3D surface plots were from the respective Scan 2 with $C_\mathrm{s} = 0.3$

The accuracy of the reconstruction is calculated by determining the Cloud to Cloud distance between the calculated surface reconstruction and the ground truth using *CloudCompare* software [29]. Additionally, the location of the calculated surface reconstruction with respect to the ground truth is determined by computing the distance of each reconstruction from the centroid of the breast (determined from ground truth).

A complete overview of the results can be seen in table III. It was found that the mean error is lowest when $C_s = 0.3$ equating to 3.78 mm for both the horizontal and the vertical probe orientations. However, a larger surface area was scanned with the probe in horizontal orientation, thus indicating that the horizontal reconstruction with $C_\mathrm{s} = 0.3$ has a higher accuracy.

With reference to figure 6, wherein the image shown represents the surface reconstruction of the probe in horizontal orientation when $C_\mathrm{s} = 0.3$, it can be seen that the error at the start of the trajectory is in the sub-mm range and increases to as high as 6 mm as the robot approaches the nipple. Thus demonstrating an increase in the reconstruction error with a decrease in the radius of curvature of the breast. The increase

Table III: A complete overview of the results including the average number of Image frames taken in each scan and the number of points in the surface reconstruction

Set Confidence Value C_s for Confidence Driven Control	**Probe Orientation**							
	Horizontal				***Vertical***			
	Average Number of Image Frames	*Mean Error (mm)*	*Std (mm)*	*Number of points after filtering*	*Average Number of Image Frames*	*Mean Error (mm)*	*Std (mm)*	*Number of points after filtering*
0.30	1277	3.78	1.71	1528	752	3.78	1.08	486
0.50	1204	7.03	1.89	702	692	5.28	1.30	402
0.65	1204	9.88	2.24	423	709	8.45	1.77	246

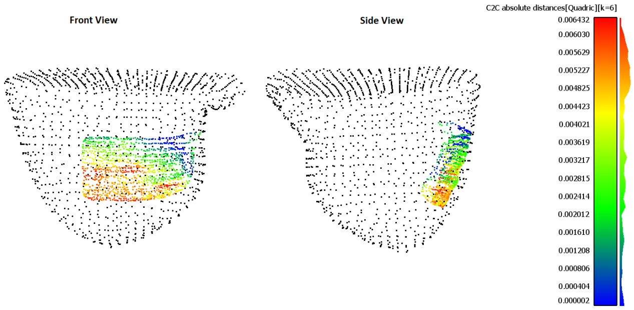

Figure 6: Error between calculated surface reconstruction with US images (multi-coloured point cloud) vs Reference Ground Truth Surface Reconstruction (black point cloud). The colour map is in meter scale. Representation is of Scan 2 with $C_s = 0.3$ and Horizontal Probe Orientation

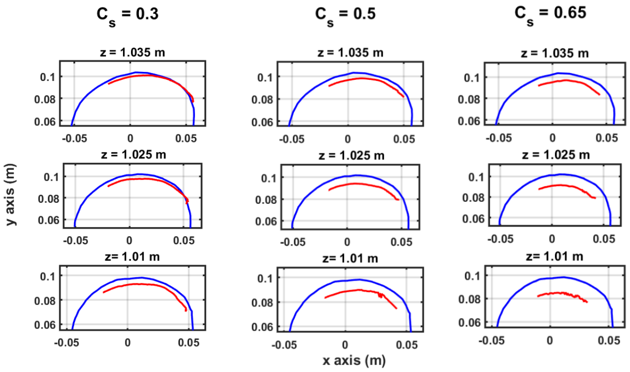

Figure 7: Slices of the $xy-$plane of the 3D reconstruction (with horizontal probe orientation) taken at different value of z to illustrate the change in occurring deformation.

in deformation with decreasing radius of curvature is further visualised in the slices of the 3D breast (along the $xy-$plane) taken at $z = 1.01$ m, $z = 1.025$ m and $z = 1.035$ m in figure 7. Furthermore, in figure 7, it can also be observed that as C_s increases, the amount of deformation increases, contributing to the increase in both the mean error and standard deviation (std) witnessed in table III.

Attributing to the tissue deformation caused by US probe forces (as seen in figures 6 and 7), it was also found that the US surface reconstruction was located inside the ground truth for all the performed experiments. The reconstruction error map as well as the image slices for the 3D reconstruction of the breast surface with a vertical probe orientation can be found in figures 14 and 15 (appendix C).

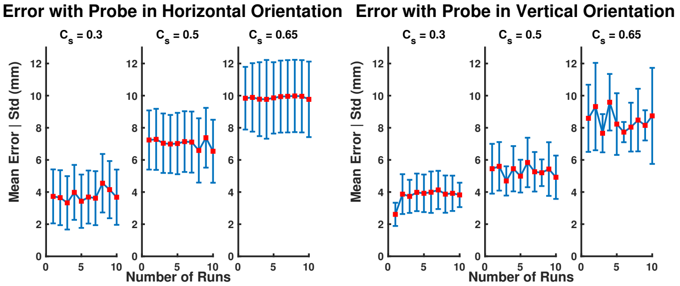

Figure 8: Error bars demonstrating the mean error and standard deviation for each experiment performed

The mean error and std for each scan can be found in figure 8. The figure indicates that the reconstruction of the breast surface with horizontal probe orientation had a similar error for all scans performed for each value of C_s, thus indicating that the reconstruction with a horizontal probe orientation has good repeatability. However, in the case of a vertical orientation, there is a larger variance in the determined error values for C_s greater than 0.3.

IV. DISCUSSION

The aim of this research is to perform 3D surface reconstruction of the breast with autonomously acquired US images. This is achieved by emphasising the regions of acoustic coupling in an US image and further extracting surface information to create a dense 3D reconstruction.

A. *Surface Reconstruction*

Due to the novel nature of the topic under study, no literature based comparison is performed with other 3D US breast surface reconstructions. Breast surface reconstruction, as mentioned in section I, is currently performed using a camera and a marker based MRI data registration system [17], and is considered to be the ground truth in this study.

Firstly, in section III-C, we demonstrated that the 3D breast surface reconstruction with US images is feasible. The effects of varying US probe orientation and C_s on the reconstruction when compared to the ground truth were also determined.

In table III, a trend of an increasing error with an increasing C_s is visible, indicating that the surface reconstruction performed with $C_s = 0.3$ resulted in the highest accuracy with a mean error of 3.87 mm. This trend thus suggests that lowering the value of C_s, could result in an improved accuracy. There will, however, be a lower limit on C_s below which surface reconstruction would not be possible, since there would be no contact between the US probe and the breast surface. It was also found that surface reconstruction was possible with $C_s = 0.5$ (as was used in previous work, Wellerweerd et. at. [20]), but with a trade-off of decreased accuracy.

Figures 6 and 7 show that the surface reconstruction error increases with a decrease in the radius of curvature. This is attributed to the additional deformation caused by the US probe in order to ensure that the desired C_s is obtained with the decreased radius.

Table III also demonstrated an increased error for a lesser amount of data acquired when performing the scans with a vertical probe orientation. This increase in error is a consequence of the instability in the PD controller that resulted in a vibration of the breast when in contact with the unstable US probe. Furthermore, the variance in the error seen in figure 8, for the vertical probe orientation, could be a result of the difference in the amount of data acquired in each scan. This is because the measurements were ended when the control turned unstable.

The algorithm for surface reconstruction takes approximately 5 seconds processing time after image acquisition and is developed on a breast phantom with a high stiffness and a large size. The stiffness of the breast tissue depends on the composition of dense and fatty tissues inside the breast. Breasts with a high fat composition have a low stiffness and are easily deformed. Independent of stiffness, for breasts of larger size, the developed algorithm should be successful. However adjustments to the image acquisition would need to be implemented in order to ensure that the data is acquired in a stable manner with minimal surface deformation. For a smaller breast size, however, adjustments would need to be implemented to the surface reconstruction algorithm. This is because as the breast size decreases, the surface tends to flatten out, resulting in a larger amount of contact between the US probe and the deformable breast.

Moreover, the ground truth reconstruction in itself had a mean error of 2.86 mm. This error could be attributed to errors in the stereo camera calibration including lens distortion or incorrect stereo matching of landmarks found in each camera image [30]. A deviation in the marker locations from the acquisition of the MR scan to that of the stereo camera as well as external deformations and ageing of the phantom could also contribute to an increase in the recosntruction error.

B. Clinical Practice

In this study, it is shown that surface reconstruction can be performed without the use of multi-modality markers. Thus, these markers can be eliminated from the workflow making it more robust for use in a clinical environment.

Furthermore, prior to US image acquisition, it is essential that acoustic gel is applied to the US probe to reduce the acoustic impedance mismatch between the US probe and the breast surface. This is because there is a high acoustic impedance mismatch at the interface of the two surfaces which results in the transmission of only a small amount of US signal through the tissue [31]. Due to the acoustic properties of the materials used in the manufacturing of the breast phantom, the application of acoustic gel was not necessary while performing the experiments in this study.

V. CONCLUSION

In this work, we proposed an algorithm for the surface reconstruction of a soft tissue, the breast, with autonomously acquired US images. This was done by emphasising the regions of acoustic coupling by using confidence maps and with image binarisation. The validation of the thresholding methods used in binarisation indicated that the Basic Automatic Thresholding Method had the highest accuracy with an average Misclassification Error, Peak Signal-to-Noise Ratio, F-Measure and Normalised Correlation Coefficient of 0.076, 12.63, 0.93 and 0.85 respectively. The breast surface reconstruction results demonstrated that a minimal error of 3.87 mm was found when the desired amount of contact was 30% the US probe width and the probe was in horizontal orientation. It was also found that the reconstruction error increased with an increase in the amount of acoustic coupling and with a decrease in the radius of curvature of the breast. The results also indicated an increased accuracy and repeatability for the reconstruction with the probe in horizontal orientation.

VI. FURTHER RESEARCH

Estimation of the amount of deformation that occurs due to probe contact forces using mathematical models such as Finite Element Model and Mass Spring Model can help in reducing the reconstruction error [32], [33]. Based on these models, a correction to the calculated surface reconstruction can be executed. Per-pixel correction for tissue deformation using non-linear extrapolation methods could also be utilised in order to find the location of the pixels in their undeformed state [34]. Alternatively, another approach is to compute the error locally per point and based on statistical sampling correct for the deformation [35].

REFERENCES

[1] Freddie Bray, Jacques Ferlay, Isabelle Soerjomataram, Rebecca L. Siegel, Lindsey A. Torre, and Ahmedin Jemal. Global cancer statistics 2020: GLOBOCAN estimates of incidence and mortality worldwide for 36 cancers in 185 countries. *CA: A Cancer Journal for Clinicians*, 68(6):394–424, 2020.

[2] Mitra Rahimzadeh, Ahmad Reza Baghestani, Mahmood Reza Gohari, and Mohamad Amin Pourhoseingholi. Estimation of the cure rate in Iranian breast cancer patients. *Asian Pacific Journal of Cancer Prevention*, 15(12):4839–4842, 2014.

[3] Institute of Medicine and National Research Council. *Mammography and Beyond: Developing Tecnologies for the Early detection of Breast Cancer*. The national Academies Press, 2001.

[4] I. Valle, D. Tramalloni, and N. L. Bragazzi. Cancer prevention: State of the art and future prospects. *Journal of Preventive Medicine and Hygiene*, 56(1):21–27, 2015.

[5] R F Brem, L Tabár, S W Duffy, M F Inciardi, J A Guingrich, B E Hashimoto, M R Lander, R L Lapidus, M K Peterson, J A Rapelyea, S Roux, K J Schilling, B A Shah, J Torrente, R T Wynn, and D P Miller. Assessing improvement in detection of breast cancer with three-dimensional automated breast US in women with dense breast tissue: The somoinsight study. *Radiology*, 274(3):663–673, 2015.

[6] Wendie A. Berg, Jeffrey D. Blume, Jean B. Cormack, Ellen B. Mendelson, Daniel Lehrer, Marcela Böhm-Vélez, Etta D. Pisano, Roberta A. Jong, W. Phil Evans, Marilyn J. Morton, Mary C. Mahoney, Linda Hovanessian Larsen, Richard G. Barr, Dione M. Farria, Helga S. Marques, and Karan Boparai. Combined screening with ultrasound and mammography vs mammography alone in women at elevated risk of breast cancer. *JAMA - Journal of the American Medical Association*, 299(18):2151–2163, 2008.

[7] Monica Morrow, Janet Waters, and Elizabeth Morris. MRI for breast cancer screening, diagnosis, and treatment. *The Lancet*, 378(9805):1804–1811, 2011.

[8] J.A. Smith and E. Andreopoulou. An overview of the status of imaging screening technology for breast cancer. *Annals of Oncology*, 15(Supplement 1):i18–i26, 2004.

[9] L. S.J. Sim, J. H.C.L. Hendriks, and S. M.C. Fook-Chong. Breast ultrasound in women with familial risk of breast cancer. *Annals of the Academy of Medicine Singapore*, 33(5):600–606, 2004.

[10] Kazuaki Nakashima, Takayoshi Uematsu, Taiyo L. Harada, Kaoru Takahashi, Seiichirou Nishimura, Yukiko Tadokoro, Tomomi Hayashi, Junichiro Watanabe, and Takashi Sugino. MRI-detected breast lesions: clinical implications and evaluation based on MRI/ultrasonography fusion technology. *Japanese Journal of Radiology*, 37(10):685–693, 2019.

[11] Martina Zanotel, Iliana Bednarova, Viviana Londero, Anna Linda, Michele Lorenzon, Rossano Girometti, and Chiara Zuiani. Automated breast ultrasound: basic principles and emerging clinical applications. *Radiologia Medica*, 123(1):1–12, 2018.

[12] Rongrong Guo, Guolan Lu, Binjie Qin, and Baowei Fei. Ultrasound Imaging Technologies for Breast Cancer Detection and Management: A Review. *Ultrasound in Medicine and Biology*, 44(1):37–70, 2018.

[13] Eric D Larson, Won-Mean Lee, Marilyn A. Roubidoux, Mitchel M Goodsitt, Chris Lashbrook, Fouzaan Zafar, Oliver D. Kripfgans, Kai Thomenius, and Paul L. Carson. Automated Breast Ultrasound: Dual-Sided Compared with Signle Sided Imaging. 42(9):2072–2082, 2016.

[14] Shogo Nakano, Miwa Yoshida, Kimihito Fujii, Kyoko Yorozuya, Yukako Mouri, Junko Kousaka, Takashi Fukutomi, Junko Kimura, Tsuneo Ishiguchi, Kazuko Ohno, Takao Mizumoto, and Michiko Harao. Fusion of MRI and sonography image for breast cancer evaluation using real-time virtual sonography with magnetic navigation: First experience. *Japanese Journal of Clinical Oncology*, 39(9):552–559, 2009.

[15] Takayoshi Uematsu, Kaoru Takahashi, Seiichiro Nishimura, Junichiro Watanabe, Seiji Yamasaki, Takashi Sugino, Takuma Oishi, Yuko Kakuda, Mutsu Sato, and Tomomi Hayashi. Real-time virtual sonography examination and biopsy for suspicious breast lesions identified on MRI alone. *European Radiology*, 26(4):1064–1072, 2016.

[16] M. K. Welleweerd, A. G. De Groot, S. O.H. De Looijer, F. J. Siepel, and S. Stramigioli. Automated robotic breast ultrasound acquisition using ultrasound feedback. *Proceedings - IEEE International Conference on Robotics and Automation*, pages 9946–9952, 2020.

[17] Marcel K. Welleweerd, FranÃ§oise J. Siepel, Vincent Groenhuis, Jeroen Veltman, and Stefano Stramigioli. Design of an end-effector for robot-assisted ultrasound-guided breast biopsies. *International Journal of Computer Assisted Radiology and Surgery*, 15(4):681–690, 2020.

[18] Athanasios Karamalis. Ultrasound Confidence Maps and Applications in Medical Image Processing. *Dissertation*, 2013.

[19] Leo Grady. Random walks for image segmentation. *IEEE Transactions on Pattern Analysis and Machine Intelligence*, 28(11):1768–1783, 2006.

[20] M K Welleweerd, A G De Groot, V Groenhuis, F J Siepel, and S Stramigioli. Out-of-plane corrections for autonomous robotic breast ultrasound acquisitions.

[21] Milan Sonka, Vaclav Hlavac, and Roger Boyle. *Image processing, analysis and machine vision*. Global Engineering: Timothy L. Anderson, 4 edition, 2015.

[22] the free Encyclopedia Wikipedia. Thresholding (image processing), 2020.

[23] Otsu and N. A threshold selection method from gray-level histograms. *IEEE Trans. on Systems, Man and Cybernetics*, 9(1):62–66, 1996.

[24] Hui Fuang Ng. Automatic thresholding for defect detection. *Pattern Recognition Letters*, 27(14):1644–1649, 2006.

[25] A Dos Anjos and H R Shahbazkia. BI-level image thresholding - A fast method. *BIOSIGNALS 2008 - Proceedings of the 1st International Conference on Bio-inspired Systems and Signal Processing*, 2:70–76, 2008.

[26] M. Portes de Albuquerque, I. A. Esquef, A. R. Gesualdi Mello, and M. Portes de Albuquerque. Image thresholding using Tsallis entropy. *Pattern Recognition Letters*, 25(9):1059–1065, 2004.

[27] Catherine S. Giess, Sughra Raza, and Robyn L. Birdwell. Distinguishing breast skin lesions from superficial breast parenchymal lesions: Diagnostic criteria, imaging characteristics, and pitfalls. *Radiographics*, 31(7):1959–1972, 2011.

[28] Laplacian smoothing - Wikipedia.

[29] CloudCompare https://www.danielgm.net/cc/.

[30] A. Belhaoua, S. Kohler, and E. Hirsch. Estimation of 3D reconstruction errors in a stereo-vision system. *Modeling Aspects in Optical Metrology II*, 7390(October 2015):73900X, 2009.

[31] Rungroj Jintamethasawat, Xiaohui Zhang, Paul L. Carson, Marilyn A. Roubidoux, and Oliver D. Kripfgans. Acoustic beam anomalies in automated breast imaging. *Journal of Medical Imaging*, 4(04):1, 2017.

[32] Yuping Duan, Weimin Huang, Huibin Chang, Wenyu Chen, Kyaw Kyar Toe, Jiayin Zhou, Tao Yang, Jiang Liu, Soo Kng Teo, Chi Wan Lim, Yi Su, Chee Kong Chui, and Stephen Chang. Modeling and Simulation of Soft Tissue. In *Abdominal Imaging*, number September, pages 221–230. 2013.

[33] John H. Hipwell, Vasileios Vavourakis, Lianghao Han, Thomy Mertzanidou, BjÃ¶rn Eiben, and David J. Hawkes. A review of biomechanically informed breast image registration. *Physics in Medicine and Biology*, 61(2):R1–R31, 2016.

[34] Shih-Yu Sun, Brian W. Anthony, and Matthew W. Gilbertson. Trajectory-based deformation correction in ultrasound images. *Medical Imaging 2010: Ultrasonic Imaging, Tomography, and Therapy*, 7629(March 2010):76290A, 2010.

[35] Bahman Jafari, Ali Khaloo, and David Lattanzi. Deformation Tracking in 3D Point Clouds Via Statistical Sampling of Direct Cloud-to-Cloud Distances. *Journal of Nondestructive Evaluation*, 36(4):1–10, 2017.

[36] Maksym Fedorchuk and Bart Lamiroy. Statistic metrics for evaluation of binary classifiers without ground-truth. *2017 IEEE 1st Ukraine Conference on Electrical and Computer Engineering, UKRCON 2017 - Proceedings*, pages 1066–1071, 2017.

[37] M Sezgin and B Sankur. Survey over Image Thresholding Techniques and Quantitative Performance Evaluation. *Journal of Electronic Imaging*, 13(1):146–165, 2004.

APPENDIX

APPENDIX A
CONFIDENCE MAPS

An illustration of the grid walk implemented for computing a confidence map can be seen in figure 9.

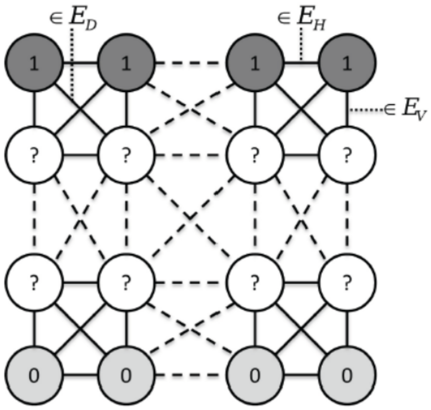

Figure 9: Representation of the random walk framework in an 8 connected graph [18].

In order to obtain the confidence map, the image is first represented as a graph $G = (V, E)$ as seen in figure 9, where nodes $v \in V$ and edges $e \in E$ [19]. An edge is basically a connection between two nodes, for instance an edge between node v_i and $v_j$is represented as e_{ij}. For an 8 connected graph, the edges can be taken in the horizontal, vertical and diagonal directions, such that $E_H \cup E_V \cup E_D = E$ where E_H, E_V, E_D represent the horizontal, vertical and diagonal edges respectively. These edges are also marked in figure 9.

Each of these edges are then assigned a weight w_{ij}, which is influenced by the three free parameters briefly described in section II-B [18]. The influence that each of these parameters has on the confidence map is as follows.

As indicated in section II, α controls the acoustic absorption and thus scales the confidence in the vertical direction. In (figure 10), it can be seen that the confidence diminishes faster in the vertical direction for a higher values of α.

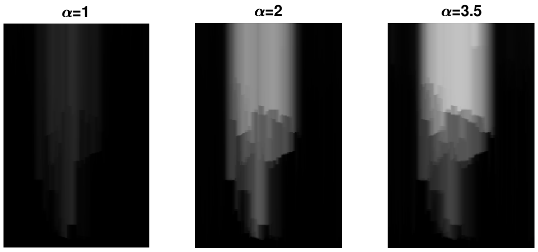
α=1 α=2 α=3.5

Figure 10: Varying α parameter, with constant $\beta = 105$ and $\gamma = 0.2$

The manipulation of β in figure 11 shows that a lower value of β, provides a lower amount of contrast, thus reducing the accuracy of segmentation.

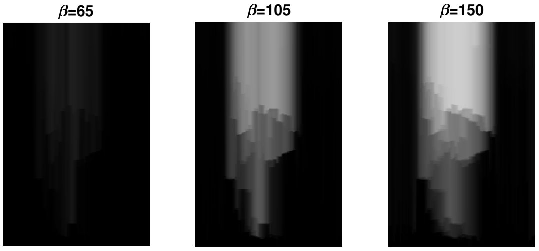
β=65 β=105 β=150

Figure 11: Varying β parameter, with constant $\alpha = 2$ and $\gamma = 0.2$

The penalty parameter γ needs to be selected such that there is a balance between the confidence and the discontinuities in the horizontal and diagonal direction. As seen in figure 12, with the increase in γ, the amount of discontinuity increases.

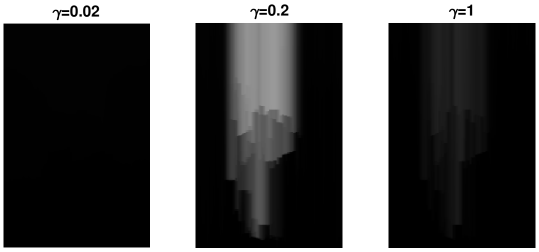
γ=0.02 γ=0.2 γ=1

Figure 12: Varying α parameter, with constant $\alpha = 2$ and $\beta = 105$

APPENDIX B
IMAGE BINARISATION

The segmentation output of each thresholding method can be seen in figure 13. The four metrics used for the validation of the binarisation method are described briefly below.

- *Metric 1*: F-Measure (FM) [36]
  F-Measure is dependent on the number of true positive (TP), false positive (FP) and false negative (FN) pixel values, and ranges between 0 and 1. It can be calculated using

$$F - Measure = \frac{2 \cdot \text{Precision} \cdot \text{Recall}}{\text{Precision} + \text{Recall}}$$

$$\text{Precision} = \frac{TP}{TP + FP} \tag{10}$$
$$\text{Recall} = \frac{TP}{TP + FN}$$

- *Metric 2:* Peak Signal to Noise Ratio (PSNR) [36]
  In binary classification, the PSNR reflects the closeness to the ground truth. It provides the ratio of the power

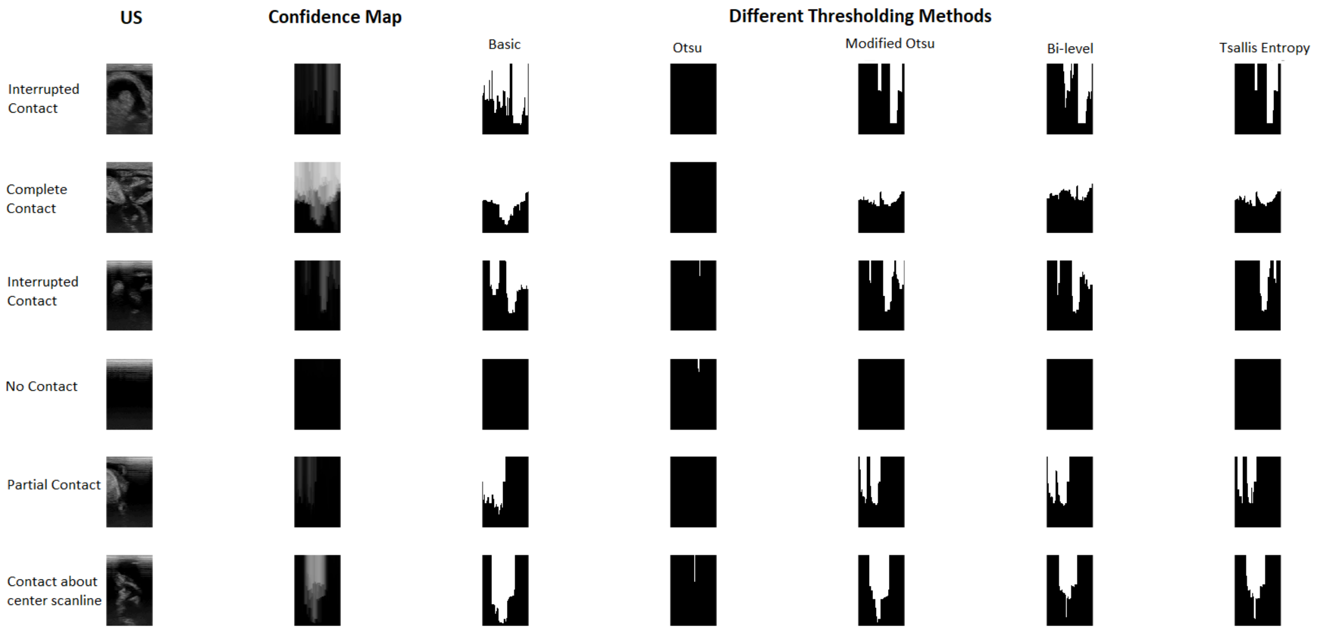

Figure 13: Binarisation of the different cases (based on the amount of contact) using different thresholding methods

of the signal to the corrupted noise in the signal. In equation (11), A, B represent the ground truth and determined binary image, c is the maximum pixel intensity difference, and $M \times N$ is the image size.

$$PSNR = 10 \cdot log_{10}(\frac{c^2}{MSE})$$
$$MSE = \frac{\sum_{m=1}^{M}\sum_{n=1}^{N}(A(m,n) - B(m,n))^2}{MN} \tag{11}$$

When the ground truth and the binarised image are identical, the PSNR will be equal to ∞.

- *Metric 3:* Misclassification Error (ME) [37]
ME indicates the number of pixels that are wrongly assigned to the background instead of the foreground and the vice versa. F_0, B_0, F_A and B_A indicate the ground truth foreground and background and the calculated foreground and background respectively.

$$\text{Misclassification Error} = 1 - \frac{|F_O \cap F_A| + |B_O \cap B_A|}{|B_O| + |F_O|} \tag{12}$$

- *Metric 4:* Normalised Correlation Coefficients (NCC) [36]
NCC finds patterns in the images and is used to find extent of similarity between two images, when considering them as multi dimensional arrays. $\bar{A}$ and $\bar{B}$ represent the mean of the array images.

$$NCC = \frac{\sum_{m=1}^{M}\sum_{n=1}^{N}(A(m,n) - \bar{A})(B(m,n) - \bar{B})}{\sqrt{\sum_{M}\sum_{N}(A(m,n) - \bar{A})^2 \sum_{M}\sum_{N}(B(m,n) - \bar{B})}} \tag{13}$$

The ME, F-Measure and NCC range between 0 and 1 while PSNR ranges from 0 to ∞. The higher the metric value for F-Measure, PSNR and NCC the better the thresholding implementation, since the calculate image provides a better estimation of the ground truth. On the contrary for ME, the lower the error, the better the implementation.

APPENDIX C
SURFACE RECONSTRUCTION

Due to the lower accuracy of the experiments performed with the US probe in Vertical Orientation, the output surface plots of the reconstruction can be found below.
The surface reconstruction of the breast with approximate distances from the ground truth is visualised in figure 14.

Table IV: Evaluation of different Binarisation techniques for different cases depending on the amount of acoustic coupling

Contact			*Evaluation Method*	*Global Thresholding Method*				
				Basic	**Otsu**	**Modified Otsu**	**Bi-Level**	**Tsallis Entropy**
No Contact			*Misclassification Error*	0.11	0.6	0.27	0.3	0.34
			PSNR	9.91	2.29	5.87	5.43	4.85
			F Measure	0.9	0.02	0.71	0.67	0.6
			NCC	0.79	0.07	0.57	0.54	0.48
Partial Contact	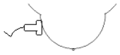	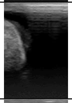	*Misclassification Error*	0.09	0.56	0.23	0.26	0.3
			PSNR	11.75	2.59	6.5	6.2	5.36
			F Measure	0.92	0.02	0.74	0.7	0.63
			NCC	0.84	0.07	0.61	0.58	0.52
Complete Contact			*Misclassification Error*	0.1	0.56	0.23	0.26	0.3
			PSNR	11.52	2.64	6.61	6.29	5.43
			F Measure	0.92	0.02	0.75	0.71	0.63
			NCC	0.83	0.07	0.62	0.59	0.52
Contact centered around the Center Scanline		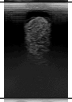	*Misclassification Error*	0.02	0.35	0.09	0.16	0.14
			PSNR	17.75	4.51	10.67	8.00	8.53
			F Measure	0.98	0.07	0.87	0.73	0.76
			NCC	0.96	0.16	0.82	0.67	0.71
Interrupted Contact		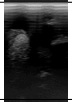	*Misclassification Error*	0.06	0.52	0.19	0.22	0.26
			PSNR	12.2	4.73	2.98	7.08	6.09
			F Measure	0.93	0.33	0.78	0.74	0.66
			NCC	0.87	0.08	0.68	0.64	0.57

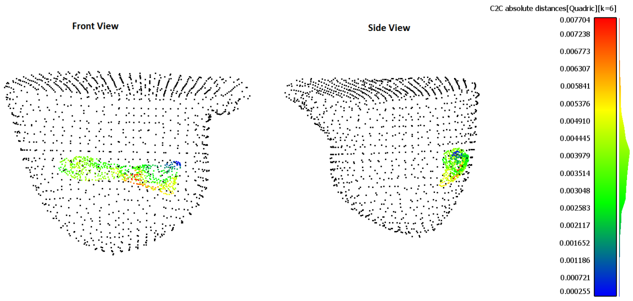

Figure 14: Error between calculated surface reconstruction with US images (multi-coloured point cloud) vs Reference Ground Truth Surface Reconstruction (black point cloud). The colour map is in meter scale. Representation is of Scan 2 with $C_s = 0.3$ and Vertical Probe Orientation

The deformation of the breast surface can be seen in the slices of the $xy-$plane of the 3D reconstruction at distinct values of z in figure 15. Due to the instability in control during image acquisition, relatively less data was acquired, thus the slices were taken at $z = 1.02$ m and 1.02 m for each value of C_s.

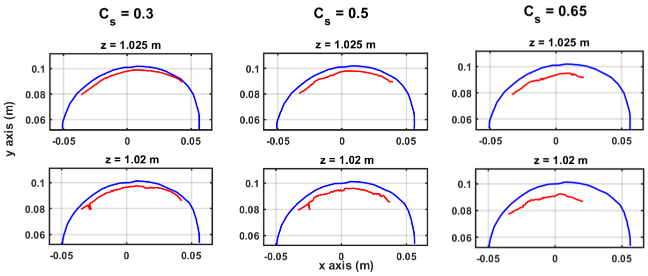

Figure 15: Slices of the $xy-$plane of the 3D reconstruction (with vertical probe orientation) taken at different value of z to illustrate the change in occurring deformation.